20th AIAA Computational Fluid Dynamics Conference
27 - 30 June 2011, Honolulu, Hawaii

AIAA 2011-3545

Rotated Hybrid Low Diffusion ECUSP-HLL scheme and Its Applications to Hypersonic Flows

Yiqing Shen* Gecheng Zha†
Dept. of Mechanical and Aerospace Engineering
University of Miami
Coral Gables, Florida 33124
E-mail: yqshen@miami.edu, gzha@miami.edu

Manuel A. Huerta‡
Dept. of Physics, University of Miami
Coral Gables, Florida 33124

Abstract

In this paper, a hybrid numerical flux scheme of low diffusion ECUSP (LDE) and HLL scheme is proposed by decomposing the cell-face normal vector. In the direction normal to shocks, the HLL scheme is applied to suppress carbuncles, in the other direction, the ECUSP scheme is implemented to keep low numerical diffusion. The new scheme with fifth-order WENO reconstruction is tested by using several benchmark cases, and then is applied to simulate a three dimensional double cone hypersonic flow of Mach number 12.43. The numerical simulation results agree very well with experiments.

Nomenclature

* Research Scientist
† Associate Professor
‡ Professor

C_k	=	optimal weight
$C^{\pm}, D^{\pm}$	=	coefficients for E-CUSP scheme
C_l^I, C_l^c, D_l^I	=	coefficients for defferencing formulas of viscous terms
IS_k	=	smoothness estimator
J	=	Jacobian of transformation
M	=	Mach number
$\mathbf{n}$	=	direction vector
Pr	=	Prandtl number
Pr_t	=	turbulent Prandtl number
p	=	pressure/power used for WENO scheme
q_k	=	heat flux in Cartesian Coordinates/3rd-order polynomial interpolation
Re	=	Reynolds number
t	=	time
u, v, w	=	velocity components in x, y and z direction
x, y, z	=	Cartesian coordinates
$\Delta\mathbf{U}$	=	difference of the conservative variables
$\Delta\mathbf{q}$	=	velocity difference vector
α, β	=	coefficients
γ	=	ratio of specific heats
ρ	=	density
μ	=	molecular viscosity
μ_t	=	turbulent viscosity
ε	=	parameter introduced in WENO scheme
ξ, η, ζ	=	generalized coordinates
ω_k	=	weight
τ	=	stress tensor
Subscripts		
i, j, k, l	=	indices
I	=	index of interface
∞	=	freestream
Superscripts		
I	=	index of interface
L, R	=	left and right sides of the interface
n	=	time level

1 Introduction

Hypersonic flow numerical simulations are very challenging due to shock anomalous solutions such as a carbuncle phenomenon. Firstly, the carbuncle is a real physical solution under some special conditions, so it is difficult to exclude by the application of any simple physical principle[1]. Secondly, the numerical anomalous phenomena depend on various factors, including geometry, mesh size, grid aspect ratio, flow Mach number, specific heat ratio and even the different accuracy order in one same solver[2]. In general, most of current remedies are *ad hoc* and are based on trial and error.

Numerical experiments show that the Rusanov solver[3] and the simplest version of the HLL Riemann solvers[4] are carbuncle free, but they obtain unacceptable solutions for shear layers due to the excessive numerical dissipation. Some other Riemann solvers, such as Roe's scheme, HLLE and HLLC schemes, and AUSM family schemes, are less dissipative, but they generate the carbuncle phenomenon. Quirk[5] proposed the idea of combining the Roe flux with the HLL flux to suppress the carbuncle problem. Recently, based on the rotated Riemann solver approach[6, 7, 8], rotated-hybrid Riemann solvers, Roe-Rusanov and Roe-HLL schemes are proposed by Nishikawa and Kitamura[9] to cure the carbuncle phenomenon. Different

from the Ren's method[8], in which the Roe's scheme is used in both directions and the carbuncle is suppressed by the dissipation introduced by the rotated flux mechanism, the rotated-hybrid schemes[9] applied a carbuncle free flux in the velocity difference direction and the Roe scheme to the other direction to prevent the flux from being too dissipative. The resulted flux can be implemented in a simple and economic manner. In addition, there are a few other methods proposed to cure the carbuncle phenomenon. For example, the modified AUSM family schemes[10, 11, 12], improved Roe scheme[1, 13], the rotated HLLC scheme and hybrid HLLC-HLL schemes[14].

In recent years, the convective upwind and split pressure (CUSP) family schemes have achieved great success. The CUSP schemes can be basically categorized to two types, the H-CUSP and E-CUSP[15, 16, 17]. The H-CUSP schemes have the total enthalpy from the energy equation in their convective vector, while the E-CUSP schemes use the total energy in the convective vector. The Liou's AUSM family schemes[18, 19, 20, 21, 22], Van Leer-Hänel scheme[23], and Edwards's LDFSS schemes[24, 25] belong to the H-CUSP group. The schemes developed by Zha, et al.[26, 27, 28, 29, 30] belong to the E-CUSP group.

From the characteristic theory point of view, the H-CUSP schemes are not fully consistent with the disturbance propagation directions[31, 32], which may affect the stability and robustness of the schemes. By splitting the eigenvalues of the Jacobians to convection (velocity) and waves (speed of sound), one will find that the convection terms only contain the total energy[26], which will lead to the E-CUSP schemes. CUSP family schemes use scalar dissipation instead of matrix dissipation such as that of the Roe's flux difference splitting scheme. Due to no matrix operation, CUSP schemes are straightforward to be generalized to multidisciplinary research, such as chemical reaction flows and magnetohydrodynamics.

In this paper, following the idea of Nishikawa and Kitamura[9], a hybrid numerical flux scheme of low diffusion ECUSP (LDE) and HLL scheme is proposed by decomposing the cell-face normal vector. In the direction normal to shocks, the HLL scheme is applied to suppress carbuncles, in the other direction, ECUSP scheme is implemented to keep low numerical diffusion. The new scheme with fifth-order WENO reconstruction is validated by using several benchmark cases, including a 3D hypersonic flow with the Mach number of 12.43 over a blunt 25°/55° double cone configuration. The numerical results agree very well with experiments.

2 Numerical Algorithm

2.1 Governing Equations

The normalized Navier-Stokes equations governing compressible viscous flows can be written in the Cartesian coordinate as:

$$\frac{\partial Q}{\partial t}+\frac{\partial E}{\partial x}+\frac{\partial F}{\partial y}+\frac{\partial G}{\partial z}=\frac{1}{Re}\left(\frac{\partial R}{\partial x}+\frac{\partial S}{\partial y}+\frac{\partial T}{\partial z}\right) \tag{1}$$

where

$$Q=\begin{bmatrix}\rho\\ \rho u\\ \rho v\\ \rho w\\ \rho e\end{bmatrix},\ E=\begin{bmatrix}\rho u\\ \rho u^2+p\\ \rho uv\\ \rho uw\\ (\rho e+p)u\end{bmatrix},\ F=\begin{bmatrix}\rho v\\ \rho uv\\ \rho v^2+p\\ \rho vw\\ (\rho e+p)v\end{bmatrix},\ G=\begin{bmatrix}\rho w\\ \rho uw\\ \rho vw\\ \rho w^2+p\\ (\rho e+p)w\end{bmatrix},$$

$$R = \begin{bmatrix} 0 \\ \tau_{xx} \\ \tau_{xy} \\ \tau_{xz} \\ u_k\tau_{xk} - q_x \end{bmatrix}, S = \begin{bmatrix} 0 \\ \tau_{xy} \\ \tau_{yy} \\ \tau_{yz} \\ u_k\tau_{yk} - q_y \end{bmatrix}, T = \begin{bmatrix} 0 \\ \tau_{xz} \\ \tau_{yz} \\ \tau_{zz} \\ u_k\tau_{zk} - q_z \end{bmatrix},$$

The repeated index k stands for the Einstein summation over x, y and z. The stress τ and heat flux q are,

$$\tau_{ik} = \mu \left[(\frac{\partial u_i}{\partial x_k} + \frac{\partial u_k}{\partial x_i}) - \frac{2}{3}\delta_{ik}\frac{\partial u_j}{\partial x_j} \right]$$

$$q_j = \frac{-\mu}{(\gamma - 1)M_\infty^2 Pr}\frac{\partial T}{\partial x_j}$$

The equation of state is

$$\rho e = \frac{p}{\gamma - 1} + \frac{1}{2}\rho(u^2 + v^2 + w^2)$$

In the above equations, ρ is density, u, v, and w are the Cartesian velocity components in x, y and z directions, p is static pressure, and e is total energy per unit mass, μ is molecular viscosity, γ, Re, M_∞, Pr and Pr_t are the ratio of specific heat, Reynolds number, freestream Mach number, Prandtl number and turbulent Prandtl number, respectively.

In the generalized computational coordinates, Eq.(1) can be written as:

$$\frac{\partial Q'}{\partial t} + \frac{\partial E'}{\partial \xi} + \frac{\partial F'}{\partial \eta} + \frac{\partial G'}{\partial \zeta} = \frac{1}{Re}\left(\frac{\partial R'}{\partial \xi} + \frac{\partial S'}{\partial \eta} + \frac{\partial T'}{\partial \zeta} \right) \tag{2}$$

where,

$$Q' = \frac{1}{J}Q,$$

$$E' = \frac{1}{J}(\xi_x E + \xi_y F + \xi_z G),$$

$$F' = \frac{1}{J}(\eta_x E + \eta_y F + \eta_z G),$$

$$G' = \frac{1}{J}(\zeta_x E + \zeta_y F + \zeta_z G),$$

$$R' = \frac{1}{J}(\xi_x R + \xi_y S + \xi_z T),$$

$$S' = \frac{1}{J}(\eta_x R + \eta_y S + \eta_z T),$$

$$T' = \frac{1}{J}(\zeta_x R + \zeta_y S + \zeta_z T).$$

where J is the transformation Jacobian. The inviscid flux E' can be written as

$$E'(\mathbf{n}) = \frac{1}{J}\begin{Bmatrix} \rho U \\ \rho u U + \xi_x p \\ \rho v U + \xi_y p \\ \rho w U + \xi_z p \\ (\rho e + p)U \end{Bmatrix},$$

where $U = \xi_x + \xi_y v + \xi_z w$. For simplicity, the prime $'$ in Eq.(2) will be omitted in the rest of this paper.

Eq.(2) is discretized in an implicit form as

$$\begin{array}{c}\frac{1}{J\Delta t}\Delta Q^{n+1}+(E^{n+1}_{i+\frac{1}{2}}-E^{n+1}_{i-\frac{1}{2}})+(F^{n+1}_{j+\frac{1}{2}}-F^{n+1}_{j-\frac{1}{2}})+(G^{n+1}_{k+\frac{1}{2}}-G^{n+1}_{k-\frac{1}{2}})= \\ \frac{1}{Re}[(R^{n+1}_{i+\frac{1}{2}}-R^{n+1}_{i-\frac{1}{2}})+(S^{n+1}_{j+\frac{1}{2}}-S^{n+1}_{j-\frac{1}{2}})+(T^{n+1}_{k+\frac{1}{2}}-T^{n+1}_{k-\frac{1}{2}})],\end{array} \tag{3}$$

where, the inviscid numerical fluxes $E^{n+1}_{i+\frac{1}{2}}$, $F^{n+1}_{j+\frac{1}{2}}$ and $G^{n+1}_{k+\frac{1}{2}}$ are evaluated by the rotated hybrid LDE-HLL scheme with the fifth-order WENO reconstruction as described in the following, and the viscous numerical fluxes $R^{n+1}_{i+\frac{1}{2}}$, $S^{n+1}_{j+\frac{1}{2}}$ and $T^{n+1}_{k+\frac{1}{2}}$ are evaluated by a 2nd or 4th order fully conservative central differencing described in Section 2.6.

2.2 The Rotated Scheme

Let $\mathbf{n}$ be an outward pointing vector normal to a grid interface. The rotated scheme for the inviscid flux is based on the decomposition of $\mathbf{n}$ into two orthogonal directions[8, 9, 14], i.e.,

$$\mathbf{n}=\alpha_{\mathbf{1}}\mathbf{n_1}+\alpha_{\mathbf{2}}\mathbf{n_2}, \qquad \mathbf{n_1}\cdot\mathbf{n_2}=\mathbf{0}, \tag{4}$$

where $\mathbf{n_1}$ and $\mathbf{n_2}$ are two unit vectors, i.e. $|\mathbf{n_1}|=|\mathbf{n_2}|=\mathbf{1}$, and $\alpha_{\mathbf{1}}=\mathbf{n_1}\cdot\mathbf{n}$, $\alpha_{\mathbf{2}}=\mathbf{n_2}\cdot\mathbf{n}$. In order to keep the same left and right states in both directions, the vectors $\mathbf{n_1}$ and $\mathbf{n_2}$ are chosen to make $\alpha_1\geq 0$ and $\alpha_2\geq 0$. The interface flux is then decomposed correspondingly into the following form:

$$E_{i+1/2}(\mathbf{n})=\alpha_1 E^1_{i+1/2}(\mathbf{n_1})+\alpha_2 E^2_{i+1/2}(\mathbf{n_2}) \tag{5}$$

Here, the currently existing rotated-type methods are listed,

(1) $E^1=E^2=E^{Roe}$, Rotated Roe's flux[8];

(2) $E^1=E^{Rusanov}$, $E^2=E^{Roe}$, Rotated hybrid RR flux[9];

(3) $E^1=E^{HLL}$, $E^2=E^{Roe}$, Rotated hybrid RHLL flux[9];

(4) $E^1=E^{HLLC}$, $E^2=E^{HLLC}$, Rotated HLLC flux[14];

(5) $E^1=E^{HLL}$, $E^2=E^{HLLC}$, Rotated hybrid HLLC-HLL flux[14].

Huang et al[14] proposed another kind of hybrid HLLC-HLL flux as,

$$E_{i+1/2}(\mathbf{n})=\beta_1 E^{HLLC}_{i+1/2}(\mathbf{n})+\beta_2 E^{HLL}_{i+1/2}(\mathbf{n})$$

where the weights $\beta_1=\frac{1}{2}+\frac{1}{2}\alpha_1/(\alpha_1+\alpha_2)$, $\beta_1=\frac{1}{2}\alpha_2/(\alpha_1+\alpha_2)$.

Due to low diffusion and matrix-operation free, the LDE scheme is used in this paper to construct a rotated hybrid LDE-HLL scheme, i.e.,

$$E_{i+1/2}(\mathbf{n})=E^{LDE-HLL}_{i+1/2}(\mathbf{n})=\alpha_1 E^{HLL}_{i+1/2}(\mathbf{n_1})+\alpha_2 E^{LDE}_{i+1/2}(\mathbf{n_2}). \tag{6}$$

A brief description of fluxes E^{LDE} and HLL will be given in the following.

To complete the construction of the rotated-type flux, the directions $\mathbf{n_1}$ and $\mathbf{n_2}$ should be determined reasonably. Ren[8] decomposed a cell-face normal into two directions: one aligned with the velocity difference vector (normal to shocks and parallel to shears) and the other orthogonal to it. That is $\mathbf{n_1}$ is chosen as,

$$\mathbf{n_1}=\begin{cases}\mathbf{n}, & if \quad ||\Delta\mathbf{q}||\leq\epsilon \\ \frac{\Delta\mathbf{q}}{||\Delta\mathbf{q}||}, & otherwise\end{cases}, \tag{7}$$

where $\Delta\mathbf{q} = (\Delta u, \Delta v, \Delta w) = (u_R - u_L, v_R - v_L, w_R - w_L)$, $||\Delta\mathbf{q}|| = \sqrt{(\Delta u)^2 + (\Delta v)^2 + (\Delta w)^2}$, ϵ is a small parameter (in this paper,$\epsilon = 10^{-6}$, and $\mathbf{n_2}$ can be calculated by

$$\mathbf{n_2} = \frac{(\mathbf{n_1} \times \mathbf{n}) \times \mathbf{n_1}}{||(\mathbf{n_1} \times \mathbf{n}) \times \mathbf{n_1}||}.$$

As pointed out by Nishikawa and Kitamura[9], it may be argued that the nonlinear instability is caused by a transverse perturbation and therefore a dissipative flux should be applied parallel to the shock[10] and also be argued that the transverse perturbation is caused by a perturbation normal to the shock, implying that a dissipative flux normal to the shock will prevent the nonlinear instability in its early stage[33]. At the same time, in order to reduce the diffusion induced by the rotated flux on the shear layer, Nishikawa and Kitamura[9] proposed to use a cell-tangent instead of normal, i.e., the direction $\mathbf{n_1}$ is determined as

$$\mathbf{n_1} = \begin{cases} \mathbf{n}_\perp, & if \quad ||\Delta\mathbf{q}|| \le \epsilon \\ \frac{\Delta\mathbf{q}}{||\Delta\mathbf{q}||}, & otherwise \end{cases}. \tag{8}$$

In this paper, Eq. (8) is used.

2.3 Low Diffusion E-CUSP (LDE) Scheme

In generalized coordinate system, the inviscid flux vector $\mathbf{E}$ can be split as the following[30]

$$\mathbf{E} = \mathbf{E}^c + \mathbf{E}^p = M \begin{pmatrix} \rho C \\ \rho u C \\ \rho v C \\ \rho w C \\ \rho e C \end{pmatrix} + \begin{pmatrix} 0 \\ l_x p \\ l_y p \\ l_z p \\ pCM \end{pmatrix}, \tag{9}$$

where

$$U = l_x u + l_y v + l_z w, \quad M = \frac{U}{C}, \quad C = c\sqrt{l_x^2 + l_y^2 + l_z^2}.$$

c is the speed of sound, $\mathbf{n} = (l_x, l_y, l_z)$ is the normal vector in ξ-direction.

Following Zha et al.[30], a numerical flux of the LDE scheme is constructed as the following,

$$\mathbf{E}_{1/2}^{LDE} = C^+ \begin{pmatrix} \rho C \\ \rho u C \\ \rho v C \\ \rho w C \\ \rho e C \end{pmatrix}_L + C^- \begin{pmatrix} \rho C \\ \rho u C \\ \rho v C \\ \rho w C \\ \rho e C \end{pmatrix}_R + p_{1/2} \begin{pmatrix} 0 \\ l_x \\ l_y \\ l_z \\ C^+ C_L + C^- C_R \end{pmatrix}, \tag{10}$$

where

$$p_{1/2} = (D_L^+ p_L + D_R^- p_R), \tag{11}$$

and

$$
\begin{aligned}
&a_{1/2} = \frac{1}{2}(C_L + C_R),\\
&M_{L,R} = \frac{U_{L,R}}{a_{1/2}},\\
&C^+ = \alpha_L^+(1+\beta_L)M_L - \frac{1}{4}\beta_L(M_L+1)^2 - M^+_{\frac{1}{2}},\\
&C^- = \alpha_R^-(1+\beta_R)M_R + \frac{1}{4}\beta_R(M_R-1)^2 + M^-_{\frac{1}{2}},\\
&\alpha^{\pm}_{L,R} = \frac{1}{2}\left[1 \pm sign(M_{L,R})\right],\\
&\beta_{L,R} = -max\left[0, 1 - int(|M_{L,R}|)\right],\\
&M^+_{\frac{1}{2}} = M_{\frac{1}{2}}\frac{C_R + C_L\Phi}{C_R + C_L},\ M^-_{\frac{1}{2}} = M_{\frac{1}{2}}\frac{C_L + C_R\Phi}{C_R + C_L},\ \Phi = \frac{(\rho C^2)_R}{(\rho C^2)_L},\\
&M_{\frac{1}{2}} = \beta_L\delta^+ M_L^- - \beta_R\delta^- M_R^+,\\
&\delta^{\pm} = \frac{1}{2}\left\{1 \pm sign\left[\frac{1}{2}\left(M_L + M_R\right)\right]\right\},\\
&D^{\pm}_{L,R} = \alpha^{\pm}_{L,R}(1+\beta_{L,R}) - \frac{1}{4}\beta_{L,R}\left(M_{L,R} \pm 1\right)^2\left(2 \mp M_{L,R}\right).
\end{aligned}
\tag{12}
$$

2.4 HLL Scheme

As used in [9], the HLL scheme employed in this paper refers to the simpler version of the two approximate Riemann solvers proposed by Harten et al.[4]. It is given by

$$
\mathbf{E}^{HLL}_{1/2} = \frac{S_R^+\mathbf{E}(\mathbf{U}_L) - S_L^-\mathbf{E}(\mathbf{U}_R)}{S_R^+ - S_L^-} + \frac{S_R^+ S_L^-}{S_R^+ - S_L^-}\Delta\mathbf{U}, \tag{13}
$$

where

$$
S_R^+ = max(0, S_R), \quad S_L^- = min(0, S_L),
$$

and

$$
S_L = min(U_L - C_L, \bar{U} - \bar{C}), \quad S_R = max(U_R + C_R, \bar{U} + \bar{C}),
$$

where $\bar{U}$, $\bar{C}$ is calculated based on the Roe-averaged values.

2.5 The WENO Reconstruction

The high order accuracy of $E_{1/2}$ is obtained by achieving the high order accuracy of the left and right conservative variables Q^L and Q^R using the WENO scheme described below. This procedure is similar to the MUSCL scheme suggested by van Leer[34].

The WENO scheme is used to evaluate the conservative variables Q^L and Q^R. The WENO scheme for a variable u^L (u^R is constructed symmetrically as u^L about $i+1/2$ and omitted here) can be written as[35]:

$$
u^L_{i+1/2} = \sum_{k=0}^{r}\omega_k q_k, \tag{14}
$$

where $\omega_k (k = 0, \cdots, r)$ are the weights, and the $q_k (k = 0, \cdots, r)$ are the rth order accuracy reconstruction of the variables in three different stencils.

$$
\omega_k = \frac{\alpha_k}{\alpha_0 + \cdots + \alpha_{r-1}}, \tag{15}
$$

where

$$\alpha_k = \frac{C_k}{(\varepsilon + IS_k)^p}, \quad k = 0, 1, 2, \tag{16}$$

and where C_k are the optimal weights with the values given below.

The smoothness indicators IS_k suggested by Jiang and Shu[35] are given by

$$IS_k = \sum_{l=1}^{r-1} \Delta x^{2l-1} \int_{x_{i-\frac{1}{2}}}^{x_{i+\frac{1}{2}}} (\frac{d^l}{dx^l} \hat{q}_k(x))^2 dx. \tag{17}$$

The ε in Eq.(16) is introduced to avoid the denominator becoming zero. Jiang and Shu's numerical tests indicate that the results are not sensitive to the choice of ε as long as it is in the range of 10^{-5} to 10^{-7}. In their paper[35], ε is taken as 10^{-6}. In [36], Shen et al suggested to use an optimized ε value of 10^{-2} in the smoothness estimators to achieve optimal weight in smooth regions in order to minimize dissipation and improve convergence.

For the third-order($r = 2$) WENO scheme, there are

$$q_0 = -\frac{1}{2}u_{i-1} + \frac{3}{2}u_i, \quad q_1 = \frac{1}{2}u_i + \frac{1}{2}u_{i+1},$$

and

$$C_0 = 1/3, \quad C_1 = 2/3,$$
$$IS_0 = (u_i - u_{i-1})^2, \quad IS_1 = (u_{i+1} - u_i)^2. \tag{18}$$

For the fifth-order($r = 3$) WENO scheme, there are

$$q_0 = \frac{1}{3}u_{i-2} - \frac{7}{6}u_{i-1} + \frac{11}{6}u_i,$$

$$q_1 = -\frac{1}{6}u_{i-1} + \frac{5}{6}u_i + \frac{1}{3}u_{i+1},$$

$$q_2 = \frac{1}{3}u_i + \frac{5}{6}u_{i+1} - \frac{1}{6}u_{i+2},$$

and

$$C_0 = 0.1, \quad C_1 = 0.6, \quad C_2 = 0.3.$$

The IS_k are

$$\begin{aligned} IS_0 &= \tfrac{13}{12}(u_{i-2} - 2u_{i-1} + u_i)^2 + \tfrac{1}{4}(u_{i-2} - 4u_{i-1} + 3u_i)^2, \\ IS_1 &= \tfrac{13}{12}(u_{i-1} - 2u_i + u_{i+1})^2 + \tfrac{1}{4}(u_{i-1} - u_{i+1})^2, \\ IS_2 &= \tfrac{13}{12}(u_i - 2u_{i+1} + u_{i+2})^2 + \tfrac{1}{4}(3u_i - 4u_{i+1} + u_{i+2})^2. \end{aligned} \tag{19}$$

2.6 The 4th-Order Schemes for Viscous Terms[37]

A set of fully conservative 4th-order accurate finite central differencing schemes using the same stencil width of the WENO scheme for the viscous terms is used in this paper. The scheme for the viscous derivative term $\frac{\partial R}{\partial \xi}$ in Navier-Stokes equations Eq.(2) can be written as the following,

$$\frac{\partial R}{\partial \xi}|_i = \frac{\tilde{R}_{i+1/2} - \tilde{R}_{i-1/2}}{\Delta \xi} \tag{20}$$

To obtain 4th order accuracy, $\tilde{R}$ needs to be reconstructed as

$$\tilde{R}_{i-1/2} = \sum_{I=i-3/2}^{i+1/2} \alpha_I R_I \tag{21}$$

where

$$\begin{aligned}
&\alpha_{i-3/2} = -\frac{1}{24},\ \alpha_{i-1/2} = \frac{26}{24},\ \alpha_{i+3/2} = -\frac{1}{24},\\
&R_{i-1/2} = \left[(\xi_x\tau_{xx}) + (\eta_y\tau_{xy}) + (\zeta_z\tau_{xz})\right]_{i-1/2},\\
&\begin{aligned}(\tau_{xx}) = \ & \mu\{\tfrac{4}{3}\left[(\xi_x\tfrac{\partial u}{\partial\xi}) + (\eta_x\tfrac{\partial u}{\partial\eta}) + (\zeta_x\tfrac{\partial u}{\partial\zeta})\right]\\ & -\tfrac{2}{3}[(\xi_y\tfrac{\partial v}{\partial\xi}) + (\eta_y\tfrac{\partial v}{\partial\eta}) + (\zeta_y\tfrac{\partial v}{\partial\zeta})\\ & (\xi_z\tfrac{\partial w}{\partial\xi}) + (\eta_z\tfrac{\partial w}{\partial\eta}) + (\zeta_z\tfrac{\partial w}{\partial\zeta})]\}.\end{aligned}
\end{aligned} \tag{22}$$

If R_I in Eq.(21) can be approximated with the accuracy order not lower than 4th order, the Taylor expansion analysis of (20) and (21) will give the following relation[37],

$$\frac{1}{\Delta\xi}(\tilde{R}_{i+1/2} - \tilde{R}_{i-1/2}) = R^{'}(\xi_i) + O(\Delta\xi^4), \tag{23}$$

so the 4th order accuracy is achieved.

In order to achieve the highest order accuracy of R_I with $I = i-3/2, i-1/2, i+1/2$, the approximation of each component in Eq. (21) using all the involved points of the WENO stencil is given below:

$$\mu_I = \sum_{l=m}^{n} C_l^I \mu_{i+l}, \tag{24}$$

$$\frac{\partial u}{\partial\xi}|_I = \frac{1}{\Delta\xi}\sum_{l=r}^{s} D_l^I u_{i+l}, \tag{25}$$

$$\frac{\partial u}{\partial\eta}|_I = \sum_{l=m}^{n} C_l^I \frac{\partial u}{\partial\eta}|_{i+l,j}, \tag{26}$$

where

$$\frac{\partial u}{\partial\eta}|_{i,j} = \frac{1}{\Delta\eta}\sum_{l=p}^{q} C_l^c u_{i,j+l}. \tag{27}$$

By choosing different ranges for $(m,n),(r,s),(p,q)$ and different coefficients C_l^I, D_l^I, C_l^c, one can obtain different order accuracy approximation to the viscous terms. The principle of choosing $(m,n),(r,s),(p,q)$ is to ensure that the approximation of $\frac{\partial R}{\partial\xi}|_i$ in Eq.(20) is a central differencing. For example, in this paper, $(m,n) = (-2,1), (r,s) = (-3,2)$, and $(p,q) = (-2,2)$ are used, and they give[37],

$$\mu_I = \sum_{l=m}^{n} C_l^I \mu_{i+l} + O(\Delta\xi^4), \tag{28}$$

$$\frac{\partial u}{\partial\xi}|_I = \frac{1}{\Delta\xi}\sum_{l=r}^{s} D_l^I u_{i+l} + O(\Delta\xi^5), \tag{29}$$

$$\frac{\partial u}{\partial\eta}|_I = \sum_{l=m}^{n} C_l^I \frac{\partial u}{\partial\eta}|_{i+l,j} + O(\Delta\xi^4, \Delta\eta^4), \tag{30}$$

Table 1: The coefficients of C_l^I

I	C_{-2}^I	C_{-1}^I	C_0^I	C_1^I
$i-3/2$	5/16	15/16	-5/16	1/16
$i-1/2$	-1/16	9/16	9/16	-1/16
$i+1/2$	1/16	-5/16	15/16	5/16

Table 2: The coefficients of D_l^I

I	D_{-3}^I	D_{-2}^I	D_{-1}^I	D_0^I	D_1^I	D_2^I
$i-3/2$	71/1920	-141/128	69/64	1/192	-3/128	3/640
$i-1/2$	-3/640	25/384	-75/64	75/64	-25/384	3/640
$i+1/2$	-3/640	3/128	-1/192	-69/64	141/128	-71/1920

where

$$\frac{\partial u}{\partial \eta}|_{i,j} = \frac{1}{\Delta\eta}\sum_{l=p}^{q} C_l^c u_{i,j+l} + O(\Delta\eta^4). \tag{31}$$

The coefficients C_l^I, D_l^I, C_l^c can be obtained by Taylor's series expansion and are given in Tables 1-3.

Shen et al [37] proved that the scheme of Eq. (20) is symmetric with respect to cell i and is of 4th-order accuracy. The symmetry of Eq. (20) satisfies the diffusion property of viscous fluxes.

2.7 Time Marching Method

The unfactored implicit Gauss-Seidel line relaxation method developed in[38, 39, 40, 41] by the authors' research group is adopted in this paper.

The implicit fluxes given in Eq. (3) are treated as follows. The inviscid fluxes defined by Eq. (6) are approximated by the LDE fluxes $E_{1/2}^{LDE}(\mathbf{n})$ (for simplicity, the subscript LDE is omitted) and expanded in Taylor's series about interface $i+1/2$,

$$\begin{aligned} E_{i+1/2}^L|^{n+1} &= E_{i+1/2}^L|^n + (\frac{\partial E}{\partial Q}|_{i+1/2}^L)|^n \Delta Q_{i+1/2}^L|^{n+1} \\ &= E_{i+1/2}^L|^n + A_{i+\frac{1}{2}}^L|^n \Delta Q_{i+1/2}^L|^{n+1}, \\ E_{i+1/2}^R|^{n+1} &= E_{i+1/2}^R|^n + (\frac{\partial E}{\partial Q}|_{i+1/2}^R)|^n \Delta Q_{i+1/2}^R|^{n+1} \\ &= E_{i+1/2}^R|^n + A_{i+\frac{1}{2}}^R|^n \Delta Q_{i+1/2}^R|^{n+1}. \end{aligned}$$

In this paper, Jacobian matrices of Van Leer's flux[34] are used as the approximations of $A_{i+\frac{1}{2}}^L|^n$ and $A_{i+\frac{1}{2}}^R|^n$. The first-order approximation is used for the implicit convective terms to enhance diagonal dominance. That is:

$$\Delta Q_{i+1/2}^L|^{n+1} = \Delta Q_i^{n+1}, \quad \Delta Q_{i+1/2}^R|^{n+1} = \Delta Q_{i+1}^{n+1}.$$

The fluxes F and G are treated in the same way. The implicit viscous fluxes R, S and T are discretized using 2nd order central differencing. Then the final implicit form is the following,

$$\bar{B}\Delta Q_{i,j,k}^{n+1} + A^+\Delta Q_{i+1,j,k}^{n+1} + A^-\Delta Q_{i-1,j,k}^{n+1} + B^+\Delta Q_{i,j+1,k}^{n+1} + B^-\Delta Q_{i,j-1,k}^{n+1} +$$

Table 3: The coefficients of C_l^c

C_{-2}^c	C_{-1}^c	C_0^c	C_1^c	C_2^c
1/12	-8/12	0	8/12	-1/12

$$C^+\Delta Q_{i,j,k+1}^{n+1} + C^-\Delta Q_{i,j,k-1}^{n+1} = RHS^n. \tag{32}$$

The Gauss-Seidel line iteration in a certain sweep direction, for example, in ξ direction assuming the sweeping from small index value to large one, can be written as

$$B^-\Delta Q_{i,j-1,k}^{n+1} + \bar{B}\Delta Q_{i,j,k}^{n+1} + B^+\Delta Q_{i,j+1,k}^{n+1} = RHS', \tag{33}$$

where

$$RHS' = RHS^n - A^+\Delta Q_{i+1,j,k}^n - A^-\Delta Q_{i-1,j,k}^{n+1} - C^+\Delta Q_{i,j,k+1}^n - C^-\Delta Q_{i,j,k-1}^{n+1}. \tag{34}$$

3 Results and Discussion

3.1 Mach 20 hypersonic flow over a cylinder

Hypersonic flow over a cylinder is a benchmark case to check the numerical anomalous carbuncle phenomenon. The numerical simulation of a Mach number 20 inviscid flow is considered in this paper. A mesh system of 240×180 is used. The mesh is shown in Fig. 1. Fig. 2 is the pressure contours. In this case, CFL=1 is used and the iteration step is up to 100000, the maximum residual is reduced $1-2$ order. Fig. 2 shows that the carbuncle phenomenon is completely suppressed by the new scheme.

3.2 Supersonic Flat Plate Boundary Layer

A steady state laminar supersonic boundary layer flow on an adiabatic flat plate is calculated to test the accuracy and convergence of the new methodology. The incoming Mach number is 2.0. The Reynolds number based on the length of the flat plate is 4.0×10^4. The Prandtl number of 1.0 is used in order to compare with the analytical solution. The computation domain is taken to be $[0, 2] \times [0, 1.6]$. The mesh size is 180×80, and a CFL number of 20 is used.

The velocity and temperature profiles shown in Figs. 3 and 4 indicate that both numerical results agree excellently with LDE scheme and the Blasius solution. For this case, the residual of the original LDE scheme can be reduced to machine zero, but the new scheme can only reduce $3-4$ order of magnitude.

3.3 Transonic Converging-Diverging Nozzle

To examine the performance of the methodology in two-dimensional transonic flow with multiple shock waves, an inviscid transonic converging-diverging nozzle is calculated. The nozzle was designed and tested at NASA and was named Nozzle A1[42]. Due to the geometric symmetry about the center line, only the upper half of the nozzle is calculated. The mesh size is 175×50. The grid is clustered near the wall. The inlet Mach number is 0.22. The CFL number 2 is used.

In Fig. 5, the comparison of the pressure coefficients at the upper wall is illustrated. The present solution agrees well with LDE result. Due to slightly higher diffusion, the new scheme removes the tiny oscillation oscillation of the LDE scheme near the wall. The pressure contours shown in Fig. 6 shows that

the new scheme capturs the shock waves and their reflections very well. As in the case of supersonic flat plate boundary layer flow, the LDE scheme can converge to machine zero, but the new scheme can only converge around 2 order of magnitude since the direction $\mathbf{n_1}$ is always slightly changed by the shock waves.

3.4 Transonic RAE2822 Airfoil

To further examine the new scheme for transonic flows, the steady state solution of the transonic RAE2822 airfoil is calculated using the Reynolds averaged Navier-Stokes equations with the Baldwin-Lomax turbulence model. The mesh size is 128×55, the freestream Mach number M_∞ is 0.729, the Reynolds number based on chord is 6.5×10^6, and the angle of attack is 2.31^o. The CFL number 2 is used. The maximum residual of the LDE scheme can be reduced by $6 - 7$ order of magnitude, but the new scheme can only reduce around 2 order of magnitude.

The comparison of the pressure coefficients in Fig. 7 shows that present result is in good agreement with the LDE result and the experiment. The pressure contours of the present scheme are shown in Fig. 8.

3.5 3D hypersonic flow over a blunt $25^\circ/55^\circ$ double cone

To further demonstrate the present scheme for 3D applications, a 3D hypersonic flow over a blunt $25^\circ/55^\circ$ double cone is calculated with full annulus. This case is Run31 in the experiments of Holden et al.[43]. The Mach number is 12.43, Reynolds number is $6.08 \times 10^4/ft$. This case is calculated using 3D laminar Navier-Stokes equations. The computational domain of $-4 \leq x \leq 11$ and $R = 10$(unit:inch) is divided into 13 blocks. The mesh size of $70 \times 30 \times 30$ is used for the central block, which is from the leading edge of the cone to the very upstream of the far field boundary with a radius of 0.25 inch; the mesh size of $380 \times 100 \times 10$ is used for other blocks, which surround the central block and the object. Fig. 9 shows a part of the wall surface meshes. For this case, $CFL = 1$ is used.

In this simulation, there is no carbuncle at the nose. Figs. 10 and 11 are the pressure contours on the wall surface and a plane of $z = 0$ calculated by the fifth order WENO scheme at an arbitrary instant. It can be seen that the shock wave is captured very well, but the solution is not axi-symmetric, which means the flow is not at a steady state. The computed results from iteration step 100000 to 200000 are compared. There is a slight and slow variation, which may indicate the low frequency oscillation of the separation caused by the shock boundary layer interaction at the region of second cone. Further study of the separated flow unsteadyness is in progress and will be reported in the final paper.

Figs. 12 and 12 are the comparison of the pressure coefficient(C_p) and the Stanton number distribution at $z = 0$ at iteration step 150000, respectively. It can be seen that the two curves from top and bottom surfaces do not fully collapse. It means that the flow is not fully steady state and axi-symmetric. By comparing the results of 5th-order WENO and 3rd-order WENO reconstruction, it is shown that the lower order reconstruction is more stable. This may be because the 3rd order scheme is more diffusive. The predicted separated region of 5th-order WENO reconstruction is larger than that of 3rd-order WENO reconstruction. The pressure coefficient of the 5th-order WENO reconstruction agrees better with experiment than that of the 3rd-order WENO reconstruction, especially in the region downstream of the joint of two cones.

4 Conclusions

A hybrid numerical flux scheme of low diffusion ECUSP (LDE) and HLL scheme is proposed by decomposing the cell-interface normal vector. In the direction normal to shocks, the HLL scheme is applied to

suppress carbuncles, in the other direction, ECUSP scheme is implemented to maintain the low numerical diffusion. The new scheme with fifth-order WENO reconstruction is validated by several benchmark cases, including the three dimensional double cone hypersonic flow at Mach number of 12.43.

Numerical results show that present scheme can remove the numerical carbuncle phenomenon and obtain almost the same low diffusion results as the LED scheme. The new scheme is shown to be effective and robust.

5 Acknowledgment

This work was supported in part by the U. S. Air Force Office of Scientific Research under Grants FA9550-09-1-0105 monitored by Dr. Robert Barker.

References

[1] K. Kitamura,P. Roe, F. Ismail, "Evaluation of Euler Fluxes for Hypersonic Flow Computations," *AIAA J.*, vol. 47, pp. 44–53, 2009.

[2] M. Pandolfi, D. D'Ambrosio , "Numerical instabilities in upwind methods: analysis and cures for the 'carbuncle' phenomenon," *Journal of Computational Physics*, vol. 166, pp. 271–301, 2001.

[3] V. V. Rusanov, "Calculation of interaction of non-steady shock waves with obstacles," *Journal of Computational and Mathematical Physics USSR* , vol. 1, pp. 267–279, 1961.

[4] A. Harten, P.D. Lax, B. van Leer, "On upstream differencing and Godunov-type schemes for hyperbolic conservation laws," *SIAM Reviews*, vol. 25, pp. 35–61, 1983.

[5] J.J. Quirk, "A contribution to the great Riemann solver debate," *International Journal for Numerical Methods in Fluids*, vol. 18, pp. 555–574, 1994.

[6] S.F. Davis, " A rotationally biased upwind difference scheme for the Euler equations," *Journal of Computational Physics*, vol. 56, pp. 65–92, 1984.

[7] D.W. Levy, K.G. Powell, B. van Leer, "Use of a rotated Riemann solver for the two-dimensional Euler equations," *Journal of Computational Physics*, vol. 106, pp. 201–214, 1993.

[8] Y.-X. Ren, "A robust shock-capturing scheme based on rotated Riemann solvers," *Computers and Fluids*, vol. 32, pp. 1379–1403, 2003.

[9] H. Nishikawa, K. Kitamura, "Very simple, carbuncle free, boundary-layer-resolving, rotated-hybrid Riemann solvers," *Journal of Computational Physics*, vol. 227, pp. 2560–2581, 2008.

[10] M. S. Liou, "Mass flux schemes and connection to shock instability," *Journal of Computational Physics*, vol. 160, pp. 623–648, 2000.

[11] Y. Wada, M. S. Liou, "An accurate and robust flux splitting scheme for shock and contact discontinuities," *SIAM Journal on Scientiifc Computing*, vol. 18, pp. 633–657, 1997.

[12] Kyu Hong Kim, Chongam Kim, Oh-Hyun Rho, "Methods for the Accurate Computations of Hypersonic Flows: I. AUSMPW+Scheme," *Journal of Computational Physics*, vol. 174, pp. 38–80, 2001.

[13] S. S. Kim, O. H. Rho, S. K. Hong, "Cures for the shock instability: development of a shock-stable Roe scheme," *Journal of Computational Physics*, vol. 185, pp. 342–374, 2003.

[14] K. B., H. Wu, H. Yu and D. Yan, "Cures for numerical shock instability in HLLC solver." Int. J. Numer. Meth. Fluids,DOI: 10.1002/fld.2217, 2010.

[15] A. Jameson, "Analysis and Design of Numerical Schemes for Gas Dynamics I: Artificial Diffusion, Upwind Biasing, Limiters and Their Effect on Accuracy and Multigrid Convergence in Transonic and Hypersonic Flow." AIAA Paper 93-3359, July, 1993.

[16] A. Jameson, "Analysis and Design of Numerical Schemes for Gas Dynamics I: Artificial Diffusion, Upwind Biasing, Limiters and Their Effect on Accuracy and Multigrid Convergence in Transonic and Hypersonic Flow," *Journal of Computational Fluid Dynamics*, vol. 4, pp. 171–218, 1995.

[17] A. Jameson, "Analysis and Design of Numerical Schemes for Gas Dynamics II: Artificial Diffusion and Discrete Shock Structure," *Journal of Computational Fluid Dynamics*, vol. 5, pp. 1–38, 1995.

[18] M.-S. Liou and C. J. Steffen, "A New Flux Splitting Scheme," *Journal of Computational Physics*, vol. 107, pp. 1–23, 1993.

[19] Y. Wada and M.-S. Liou, "An Accurate and Robust Splitting Scheme for Shock and Contact Discontinuities." AIAA Paper 94-0083, 1994.

[20] M.-S. Liou, "Progress Towards an Improved CFD Methods: AUSM$^+$." AIAA Paper 95-1701-CP, June, 1995.

[21] M.-S. Liou, "A Sequel to AUSM: AUSM$^+$," *Journal of Computational Physics*, vol. 129, pp. 364–382, 1996.

[22] M.-S. Liou, "Ten Years in the Making-AUSM-Family." AIAA 2001-2521, 2001.

[23] D. Hänel, R. Schwane, G. Seider, "On the Accuracy of Upwind Schemes for the Solution of the Navier-Stokes Eqautions." AIAA paper 87-1105 CP, 1987.

[24] J. R. Edwards, "A Low-Diffusion Flux-Splitting Scheme for Navier-Stokes Calculations." AIAA Paper 95-1703-CP, June, 1995.

[25] J. R. Edwards, "A Low-Diffusion Flux-Splitting Scheme for Navier-Stokes Calculations," *Computer & Fluids*, vol. 6, pp. 635–659, 1997.

[26] G. -C. Zha, E. Bilgen, "Numerical Solutions of Euler Equations by Using a New Flux Vector Splitting Scheme ," *International Journal for Numerical Methods in Fluids*, vol. 17, pp. 115–144, 1993.

[27] G.-C. Zha, "Numerical Tests of Upwind Scheme Performance for Entropy Condition ," *AIAA Journal*, vol. 37, pp. 1005–1007, 1999.

[28] G.-C. Zha, "Comparative Study of Upwind Scheme Performance for Entropy Condition and Discontinuities." AIAA Paper 99-CP-3348, June 28- July 1, 1999.

[29] G.-C. Zha and Z.-J. Hu, "Calculation of Transonic Internal Flows Using an Efficient High Resolution Upwind Scheme," *AIAA Journal*, vol. 42, No. 2, pp. 205–214, 2004.

[30] G.-C. Zha, Y.-Q. Shen, B.-Y. Wang, "Calculation of Transonic Flows Using WENO Method with a Low Diffusion E-CUSP Upwind Scheme." AIAA Paper 2008-0745, Jan 2008.

[31] G.-C. Zha, "A Low Diffusion Efficient Upwind Scheme ," *AIAA Journal*, vol. 43, pp. 1137–1140, 2005.

[32] G.-C. Zha, "A Low Diffusion E-CUSP Upwind Scheme for Transonic Flows." AIAA Paper 2004-2707, to appear in AIAA Journal, 34th AIAA Fluid Dynamics Conference, June 28 - July 1 2004.

[33] P. Roe, H. Nishikawa, F. Ismail, L. Scalabrin, "On carbuncles and other excrescences." 17th AIAA Computational Fluid Dynamics Conference, AIAA Paper 2005-4872, Toronto, 2005.

[34] B. van Leer, "Towards the ultimate conservative difference scheme, III," *Journal of Computational Physics*, vol. 23, pp. 263–75, 1977.

[35] G.-S. Jiang, C.-W. Shu, "Efficient implementation of weighted ENO schemes," *J.Comput.Phys.*, vol. 126, pp. 202–228, 1996.

[36] Y.-Q. Shen, G.-C. Zha, B.-Y. Wang, "Improvement of stability and accuracy of implicit WENO scheme," *AIAA Journal*, vol. 47, pp. 331–344, 2009.

[37] Y.-Q. Shen, G.-Z. Zha, X.-Y. Chen , "High order conservative differencing for viscous terms and the application to vortex-induced vibration flows," *Journal of Computational Physics*, vol. 228, pp. 8283–8300, 2009.

[38] Z. Hu, G. -C Zha, "Calculations of 3D compressible using an efficient low diffusion upwind scheme," *International Journal for Numerical Methods in Fluids*, vol. 47, pp. 253–269, 2005.

[39] Z. J. Hu, " Parallel computation of fluid-structural interactions using high resolution upwind schemes." Ph.D. Thesis, Dept. of Mech. Aero. Eng., Univ. of Miami, May 2005.

[40] X. Chen, G. -C Zha, "Fully coupled fluid-structural interactions using an efficient high solution upwind scheme," *Journal of Fluid and Structure*, vol. 20, pp. 1105–1125, 2005.

[41] Y.-Q. Shen, B.-Y. Wang, G.-C. Zha, "Comparison study of implicit Gauss-Seidel line iteration method for transonic flows." AIAA-2007-4332, June 2007.

[42] Mason, M. L. and Putnam, L. E. , "The Effect of Throat Contouring on Two-Dimensional Converging-Diverging Nozzles at Static Conditions ." NASA Technical Paper 1704, 1980.

[43] Holden, M. S., and Wadhams, T. P., and Harvey, J. K., and Candler, G. V., "Comparisons Between DSMC and Navier-Stokes Solutions and Measurements in Regions of Laminar Shock Wave Boundary Layer Interaction in Hypersonic Flows." AIAA-2002-0435, Jan. 2002.

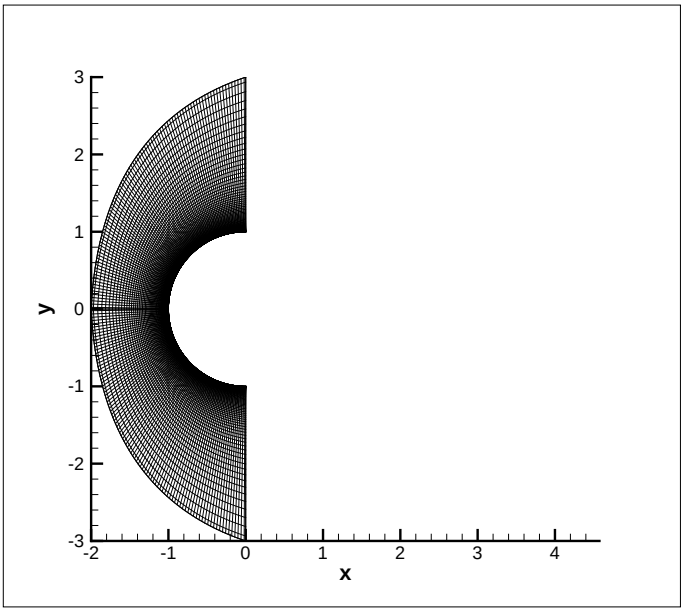

Figure 1: Sketch of mesh

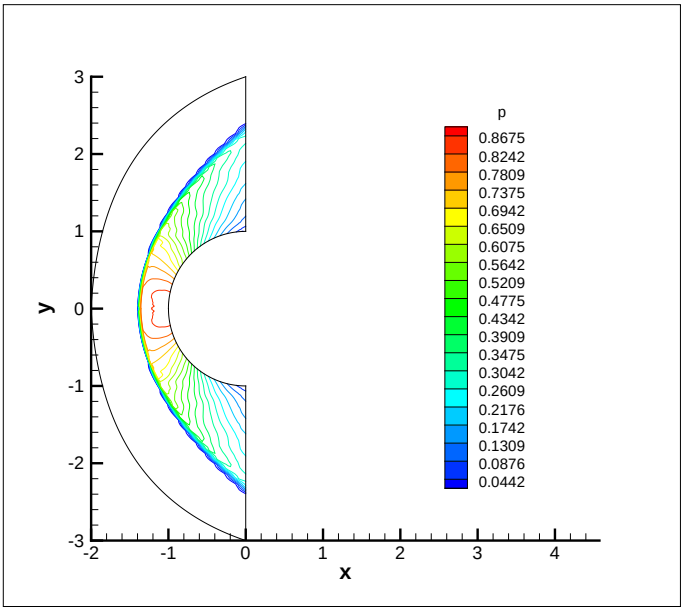

Figure 2: Pressure contours

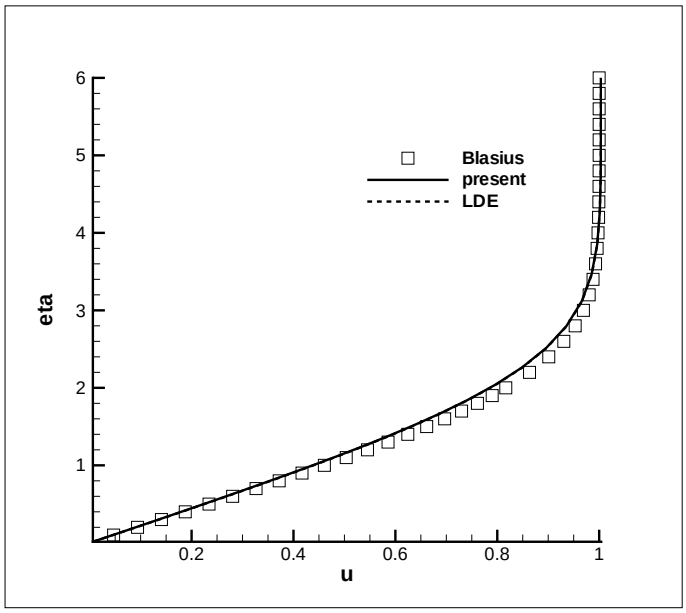

Figure 3: The velocity profiles of the supersonic laminar boundary layer flows

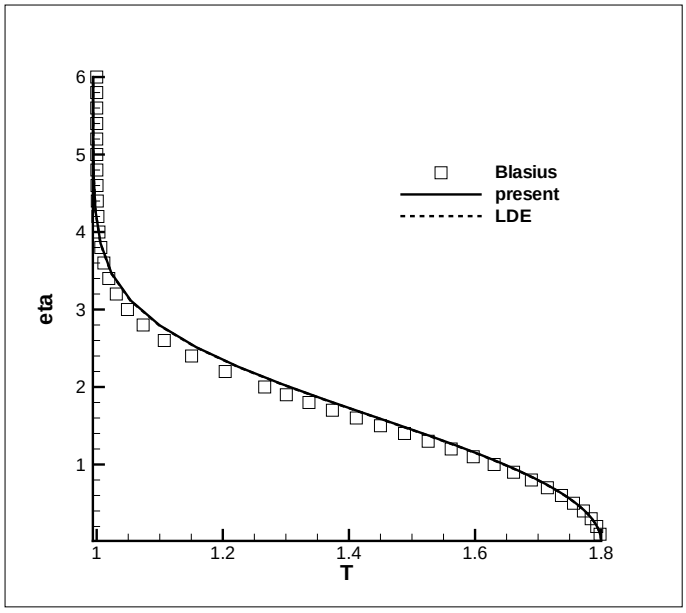

Figure 4: The temperature profiles of the supersonic laminar boundary layer flows

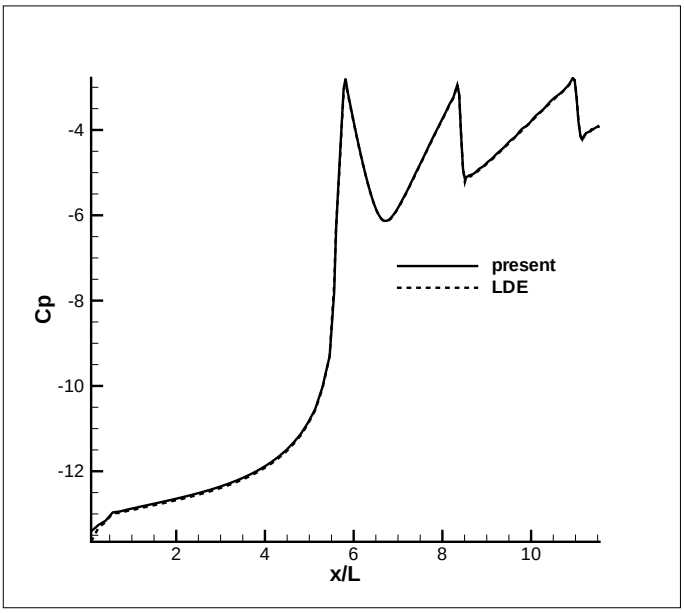

Figure 5: Comparison of the pressure coefficients at the upper wall of the transonic converging-diverging nozzle flows

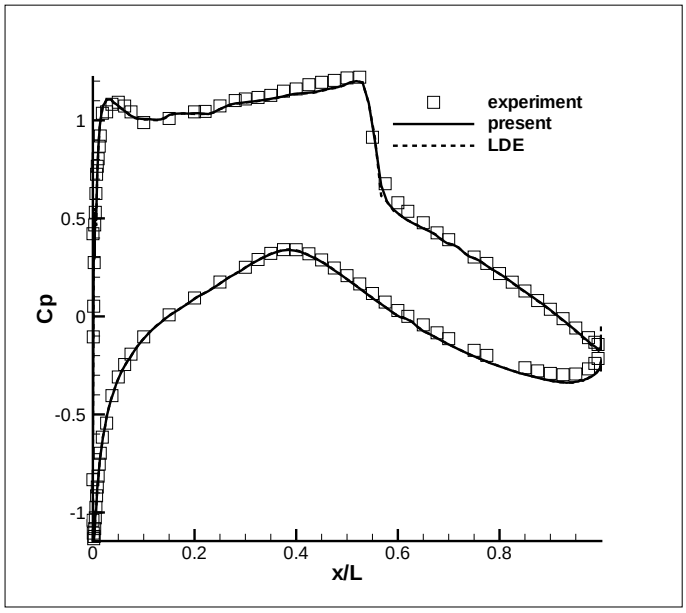

Figure 7: Pressure coefficients at the airfoil surface of the transonic flow for RAE2822 airfoil

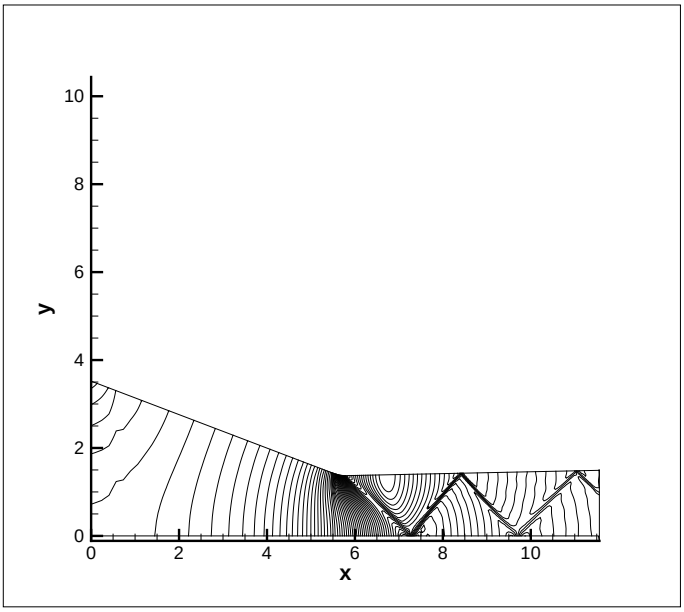

Figure 6: Pressure contours of the transonic converging-diverging nozzle flows, present method

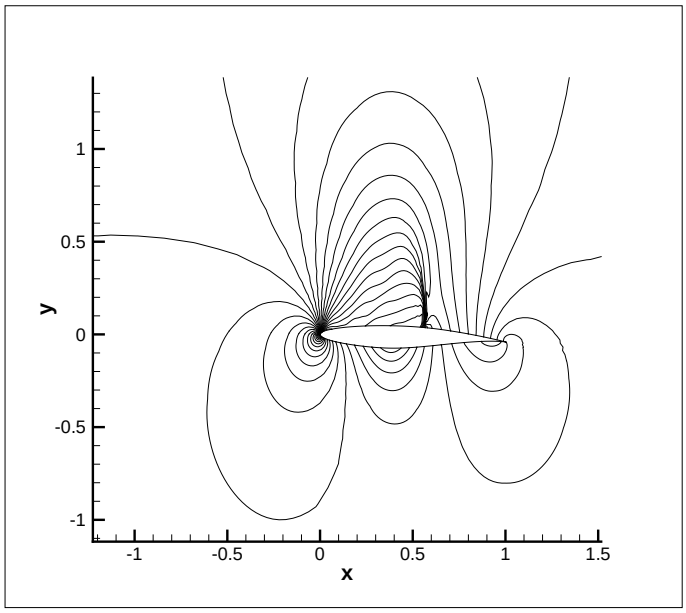

Figure 8: Pressure contours of the transonic flow for RAE2822 airfoil, present method

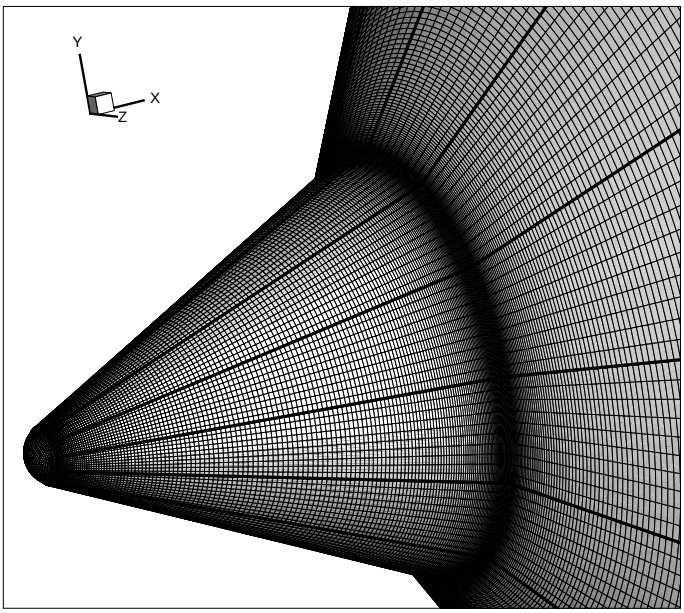

Figure 9: Sketch of multi-block grids on the double cone surface

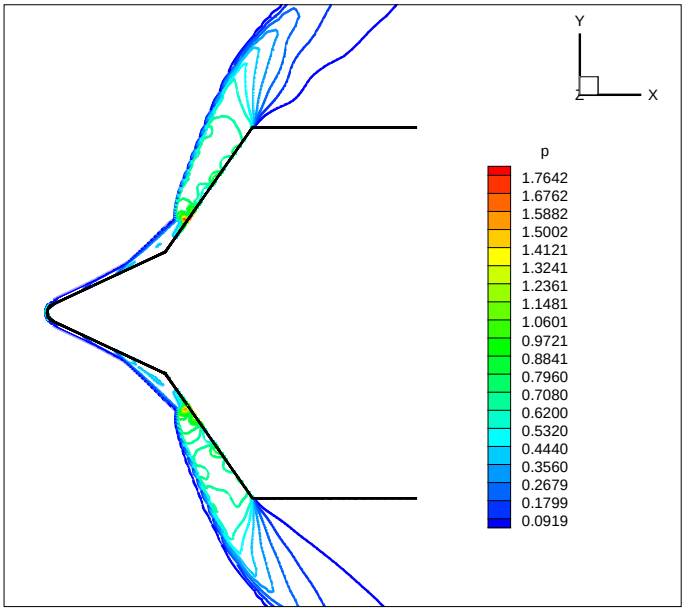

Figure 11: Pressure contours on the plane of $z = 0$, WENO-5

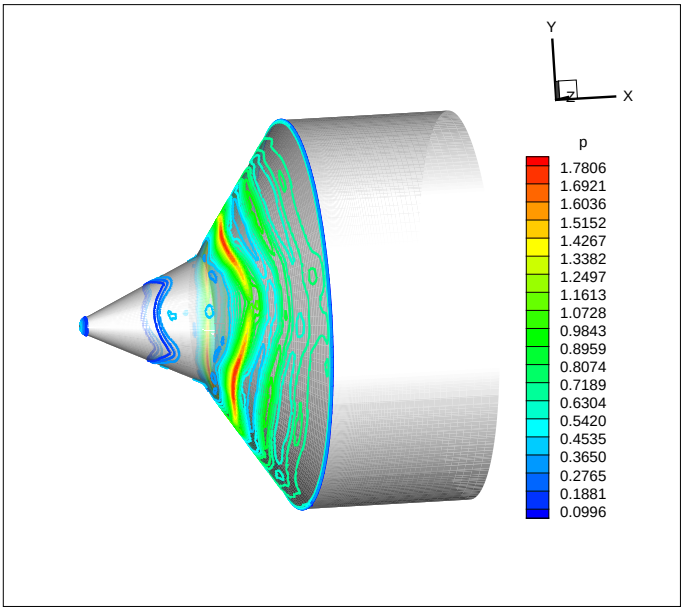

Figure 10: Pressure contours on the wall

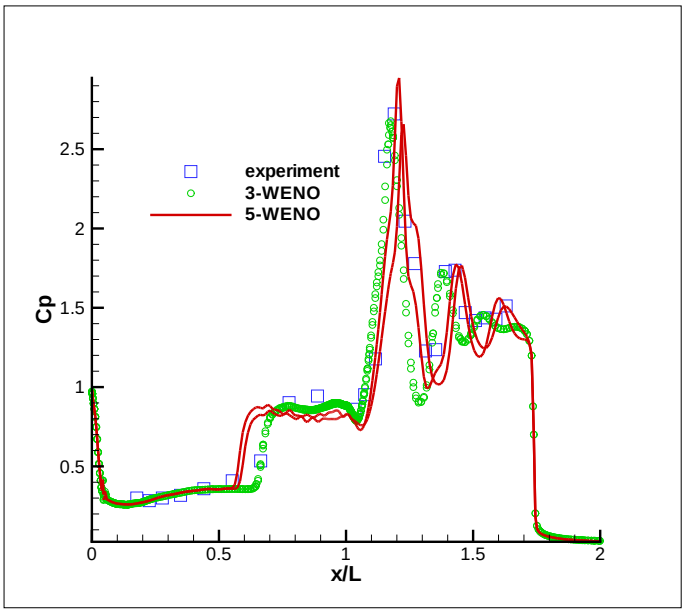

Figure 12: Comparison of pressure coefficients on wall

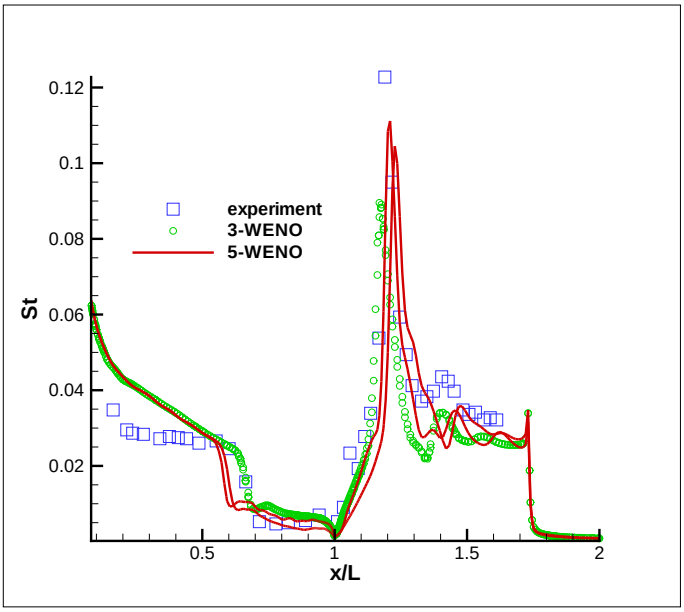

Figure 13: Comparison of Stanton number on wall